

# Effects of current on wind waves in strong winds

*Naohisa Takagaki<sup>1</sup>, Naoya Suzuki<sup>2</sup>, Yuliya Troitskaya<sup>3</sup>, Chiaki Tanaka<sup>2</sup>,  
Alexander Kandaurov<sup>3</sup>, Maxim Vdovin<sup>3</sup>*

<sup>1</sup> (Corresponding Author) Department of Mechanical Engineering, University of Hyogo,  
Shosha 2167, Himeji Hyogo, 671-2280 Japan, *E-mail: takagaki@eng.u-hyogo.ac.jp*  
Tel/Fax: +81-79-267-47834

<sup>2</sup> Faculty of Science and Engineering, Kindai University, 3-4-1, Kowakae Higashiosaka  
Osaka, 577-8502 Japan.

<sup>3</sup> Department of Geophysical Research, Institute of Applied Physics, the  
Russian Academy of Sciences, 46 Ul'yanov Street, Nizhny Novgorod, 603-950,  
Russia.

**Keywords:** wind waves, current, Doppler shift

## **Abstract**

It is important to investigate the effects of current on wind waves, called the Doppler shift, both at normal and extreme high wind speeds. Three different types of wind-wave tanks along with a fan and pump are used to demonstrate wind waves and currents in laboratories at Kyoto University, Japan, Kindai University, Japan, and the Institute of Applied Physics, Russian Academy of Sciences, Russia. Profiles of the wind and current velocities and the water-level fluctuation are measured. The wave frequency, wavelength, and phase velocity of the significant waves are calculated, and the water velocities at the water surface and in the bulk of the water are also estimated by the current distribution. The study investigated 27 cases with the measurements of winds, waves, and currents, at wind speeds ranging from 7 to 67 m s<sup>-1</sup>. At normal wind speeds under 30 m s<sup>-1</sup>, wave frequency, wavelength, and phase velocity depend on wind speed and fetch. The effect of the Doppler shift is confirmed at normal wind speeds, i.e., the significant waves are accelerated by the surface current. The phase velocity can be represented as the sum of the surface current and artificial phase velocity, which is estimated by the dispersion relation of the deep-water waves. At extreme high wind speeds, over 30 m s<sup>-1</sup>, a similar Doppler shift is observed as under the conditions of normal wind speeds. This suggests that the Doppler shift is an adequate model for representing the acceleration of wind

35 waves by current, not only for the wind waves at normal wind speeds but also for those  
36 with intensive breaking at extreme high wind speeds. A weakly nonlinear model of  
37 surface waves at a shear flow is developed. It is shown that it describes well the  
38 dispersion properties of not only small-amplitude waves but also strongly nonlinear and  
39 even breaking waves, typical for extreme wind conditions (over  $30 \text{ m s}^{-1}$ ).

40

## 41 **1. Introduction**

42 The oceans flow constantly, depending on the rotation of the Earth, tides, topography,  
43 and wind shear. High-speed continuous ocean flows are called currents. Although the  
44 mean surface velocity of the ocean is approximately  $0.1 \text{ m s}^{-1}$ , the maximum current  
45 surface velocity is more than  $1 \text{ m s}^{-1}$  (e.g., Kawabe, 1988; Kelly et al., 2001). The  
46 interaction between the current and wind waves generated by wind shear have been  
47 investigated in several studies. The acceleration effects of the current on wind waves,  
48 called the Doppler shift; the effects of the current on the momentum and heat transfer  
49 across the sea surface; and the modeling of waves and currents in the Gulf Stream have  
50 been the subject of experimental and numerical investigations (e.g., Dawe and Thompson,  
51 2006; Kara et al., 2007; Fan et al., 2009; Shi and Bourassa, 2019). Thus, wind waves  
52 follow the dispersion relationship and Doppler shift effect at normal wind speeds.  
53 However, these studies were performed at normal wind speeds only, and few studies have  
54 been conducted at extreme high wind speeds, for which the threshold velocity is  $30 - 35$   
55  $\text{m s}^{-1}$ , representing the regime shift of the air-sea momentum, heat, and mass transport  
56 (Powell et al., 2003; Donelan et al., 2004; Takagaki et al., 2012, 2016; Troitskaya et al.,  
57 2012, 2020; Iwano et al., 2013; Krall and Jähne, 2014; Komori et al., 2018; Krall et al.,  
58 2019). At such extremely high wind speeds, the water surface is intensively broken by  
59 the strong wind shear, along with the foam layer, dispersed droplets, and entrained  
60 bubbles (e.g. Donelan et al., 2004; Troitskaya et al., 2012, 2017, 2018a, 2018b; Takagaki  
61 et al., 2012, 2016; Holthuijsen et al., 2012). It is unclear if the properties of wind waves  
62 and the surface foam layer at extremely high wind speeds are similar to those at normal  
63 wind speeds. Furthermore, in a hurricane, the local ocean flows may be unusually strong,  
64 change rapidly, and strongly affect wind waves. However, the effects of the current on  
65 wind waves have not yet been clarified.

66 Therefore, the purpose of this study is to investigate the effects of the current on wind  
67 waves in strong winds through the application of three different types of wind-wave tanks,  
68 along with a pump.

69

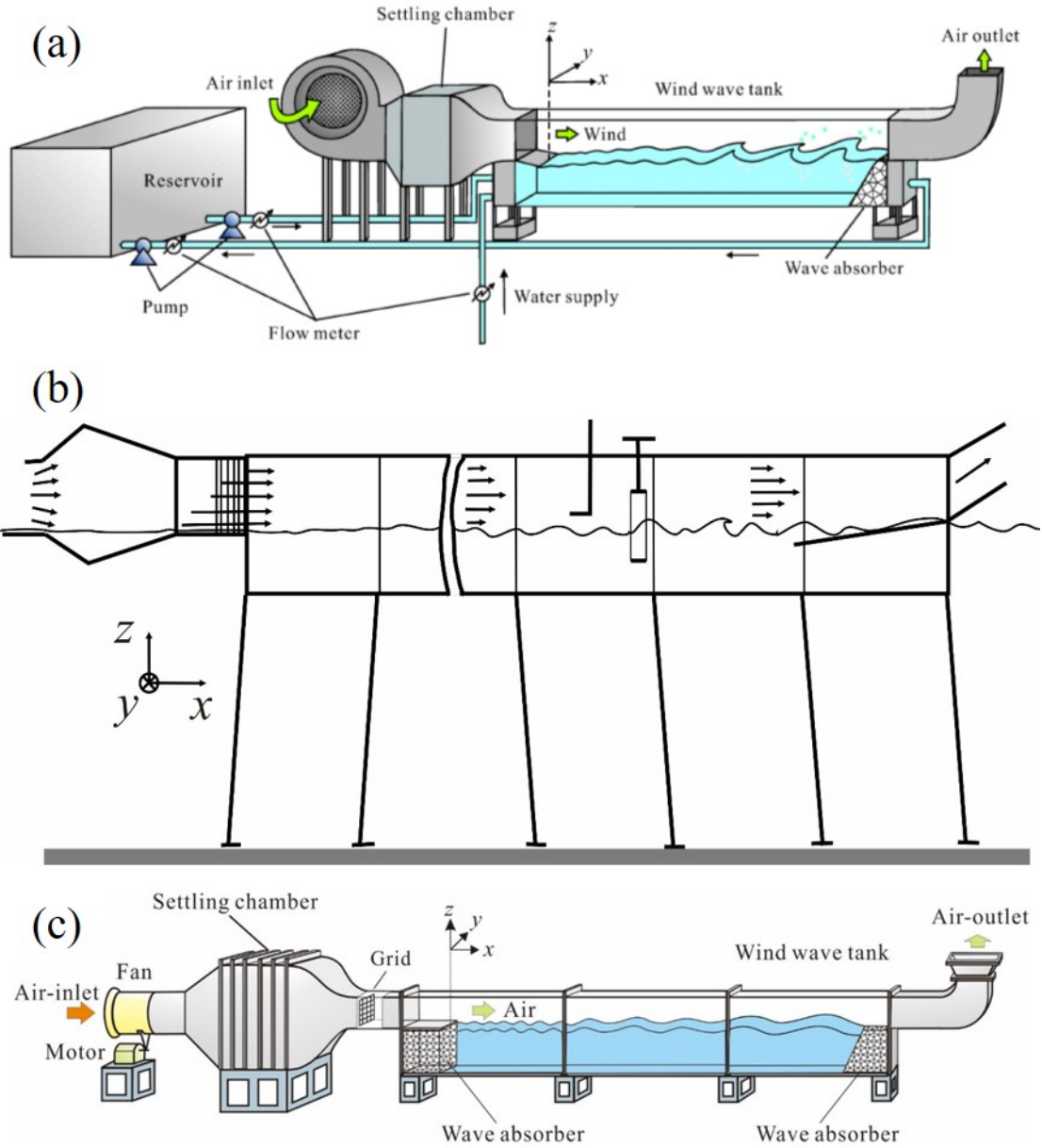


**Figure 1.** Schematics of wind-wave tanks. (a) High-speed wind-wave tank of Kyoto University. (b) Typhoon simulator of IAP RAS. (c) Wind-wave tank of Kindai University.

**2. Experiment**

**2.1. Equipment and measurement methods**

Wind-wave tanks at Kyoto University, Japan and the Institute of Applied Physics, Russian Academy of Sciences (IAP RAS) were used in the experiments (Figs. 1a, 1b). For the tank at Kyoto University, the glass test section was 15 m long, 0.8 m wide, and 1.6 m high. The water depth  $D$  was set at 0.8 m. For the tank at IAP RAS, the test section in

81 the air side was 15 m long, 0.4 m wide, and 0.4 m high. The water depth  $D$  was set at 1.5  
82 m. The wind was set to blow over the filtered tap water in these tanks, generating wind  
83 waves. The wind speeds ranged from 4.7 to 43  $\text{m s}^{-1}$  and from 8.5 to 21  $\text{m s}^{-1}$  in the tanks  
84 at Kyoto and IAP RAS, respectively. Measurements of the wind speeds, water-level  
85 fluctuation, and current were carried out 6.5 m downstream from the edge ( $x = 0$  m) in  
86 both the Kyoto and IAP RAS tanks. Here, the  $x$ ,  $y$ , and  $z$  coordinates are referred to as the  
87 streamwise, spanwise, and vertical directions, respectively, with the origin located at the  
88 center of the edge of the entrance plate. Additionally, the fetch ( $x$ ) is defined as the  
89 distance between the origin and measurement point ( $x = 6.5$  m).

90 In Kyoto, a laser Doppler anemometer (Dantec Dynamics LDA) and phase Doppler  
91 anemometer (Dantec Dynamics PDA) were used to measure the wind velocity fluctuation.  
92 A high-power multi-line argon-ion ( $\text{Ar}^+$ ) laser (Lexel model 95-7; laser wavelengths of  
93 488.0 and 514.5 nm) with a power of 3 W was used. The  $\text{Ar}^+$  laser beam was shot through  
94 the sidewall (glass) of the tank. Scattered particles with a diameter of approximately  $1 \mu\text{m}$   
95 were produced by a fog generator (Dantec Dynamics F2010 Plus) and were fed into the  
96 air flow over the waves (see Takagaki et al. (2012) and Komori et al. (2018) for details).  
97 The wind speed values ( $U_{10}$ ) at a height of 10 m height above the ocean and the friction  
98 velocity ( $u^*$ ) were estimated by the eddy correlation method, by which the mean velocity  
99 ( $U$ ) and the Reynolds stress ( $-uv$ ) in air were measured. The  $u^*$  was estimated by an eddy  
100 correlation method as  $u^* = (-\langle uv \rangle)^{1/2}$ , because the shear stress at the interface ( $\tau$ ) was  
101 defined by  $\tau = \rho u^{*2} = \rho C_D U_{10}^2$ . The value of  $(-\langle uv \rangle)^{1/2}$  was estimated by extrapolating the  
102 measured values of the Reynolds stress to the mean surface of  $z = 0$  m. The  $U_{10}$  was  
103 estimated by the log-law:  $U_{10} - U_{\min} = u^*/\kappa \ln(z_{10}/z_{\min})$ , where  $U_{\min}$  is the air velocity  
104 nearest the water surface ( $z_{\min}$ ) and  $z_{10}$  is 10 m. Moreover, the drag coefficient  $C_D$  was  
105 estimated by  $C_D = (u^*/U_{10})^2$ .

106 Water level fluctuations were measured using resistance-type wave gauges (Kenek  
107 CHT4-HR60BNC) in Kyoto. The resistance wire was placed into the water, and the  
108 electrical resistance at the instantaneous water level was recorded at 500 Hz for 600 s  
109 using a digital recorder (Sony EX-UT10). The energy of the wind waves ( $E$ ) was  
110 estimated by integrating the spectrum of the water-level fluctuations over the frequency  
111 ( $f$ ). The values of the wavelength ( $L_s$ ) and phase velocity ( $C_s$ ) were estimated using the  
112 cross-spectrum method (e.g., Takagaki et al., 2017) (see the detail in Appendix). The  
113 current was measured using the same LDA system.

114 In IAP RAS, a hot-wire anemometer (E+E Elektronic EE75) was used to measure the  
115 representative mean wind velocity at  $x = 0.5$  m and  $z = 0.2$  m. The three wind velocities  
116 ( $U_{10}$ ,  $u^*$ ,  $U_\infty$ ) at  $x = 6.5$  m were taken from Troitskaya et al. (2012) by a Pitot tube. Here,

117  $U_\infty$  is the freestream wind speed. The  $u^*$  was estimated by a profile method considering  
 118 the profiles in the constant flux layer and the wake region:

$$U_\infty - U(z) = u^* \left( -\frac{1}{\kappa} \ln(z/\delta) + \alpha \right); z/\delta < 0.15, \quad (1)$$

119

$$U_\infty - U(z) = \beta u^* (1 - z/\delta)^2; z/\delta > 0.15, \quad (2)$$

120

121 respectively. Here,  $\delta$  is the boundary layer thickness, and  $\alpha$  and  $\beta$  are the constant values  
 122 that depend on flow fields and are calibrated at low wind speeds without the dispersed  
 123 droplets. At extremely high wind speeds, measuring the profile in the constant flux layer  
 124 (Eq. 1) is difficult because of the large waves; thus, using  $\beta$  measured at low wind speeds,  
 125  $u^*$  is estimated by Eq. (2). The value of  $U_{10}$  is estimated by Eq. (1) at  $z_{10} = 10$  m with  
 126 measured  $\alpha$  at normal wind speeds. The value of  $C_D$  is estimated by  $C_D = (u^*/U_{10})^2$ .  
 127 Although the measurement methods for  $u^*$ ,  $U_{10}$ , and  $C_D$  in IAP RAS and Kyoto are  
 128 different, the values approximately correspond to each other (see Troitskaya et al. (2012)  
 129 and Takagaki et al. (2012)).

130 The water-level fluctuations were measured using three handmade capacitive-type  
 131 wave gauges in IAP RAS. Three wires formed a triangle with 25 mm on a side  
 132 ( $x$ -directional distance between wires  $\Delta x$  is 21.7 mm). The wires were placed in the water,  
 133 and the output voltages at the instantaneous water level were recorded at 200 Hz for 5400  
 134 s using a digital recorder through an AD converter (L-Card E14-140). The values ( $E$ ,  $f_m$ ,  
 135  $H_s$ ,  $T_s$ ,  $C_s$ , and  $L_s$ ) were estimated by the same manner as in Kyoto tank. The current was  
 136 measured through acoustic Doppler velocimetry (Nortec AS) at  $x = 6.5$  m and  $z = -10$ ,  
 137  $-30$ ,  $-50$ ,  $-100$ ,  $-150$ ,  $-220$ , and  $-380$  mm (see Troitskaya et al. (2012) for details).

138

## 139 **2.2. Artificial current experiments at Kindai University**

140 Additional experiments were performed using a wind-wave tank at Kindai  
 141 University with a glass test section 6.5 m long, 0.3 m wide, and 0.8 m high (Fig. 1c) (e.g.  
 142 Takagaki et al., 2020). The water depth  $D$  was set at 0.49 m. A Pitot tube (Okano Works,  
 143 LK-0) and differential manometers (Delta Ohm HD402T) were used to measure the mean  
 144 wind velocity. The values of  $u^*$ ,  $U_{10}$ , and  $C_D$  (Cases 21-27) were estimated using  $U_\infty$  by  
 145 the empirical curve by Iwano et al. (2013), which was proposed by the eddy correlation  
 146 method used in Kyoto (see section 2.1).

147 The water level fluctuations were measured using resistance-type wave gauges  
 148 (Kenek CHT4-HR60BNC). To measure  $L_s$  and  $C_s$ , another wave gauge was fixed  
 149 downstream at  $\Delta x = 0.02$  m, where  $\Delta x$  is the interval between the two wave gauges. The  
 150 values ( $E$ ,  $f_m$ ,  $H_s$ ,  $T_s$ ,  $C_s$ , and  $L_s$ ) were estimated by the same manner as in Kyoto tank.  
 151 The current was then measured through electromagnetic velocimetry (Kenek LP3100)

152 with a probe (Kenek LPT-200-09PS) at  $x = 4.0$  m. The probe sensing station was 22 mm  
153 long with a diameter of 9 mm. The measurements were performed at  $z = -15$  to  $-315$  mm  
154 at 30 mm intervals. The sampling frequency was 8 Hz, and the sampling time was 180 s.

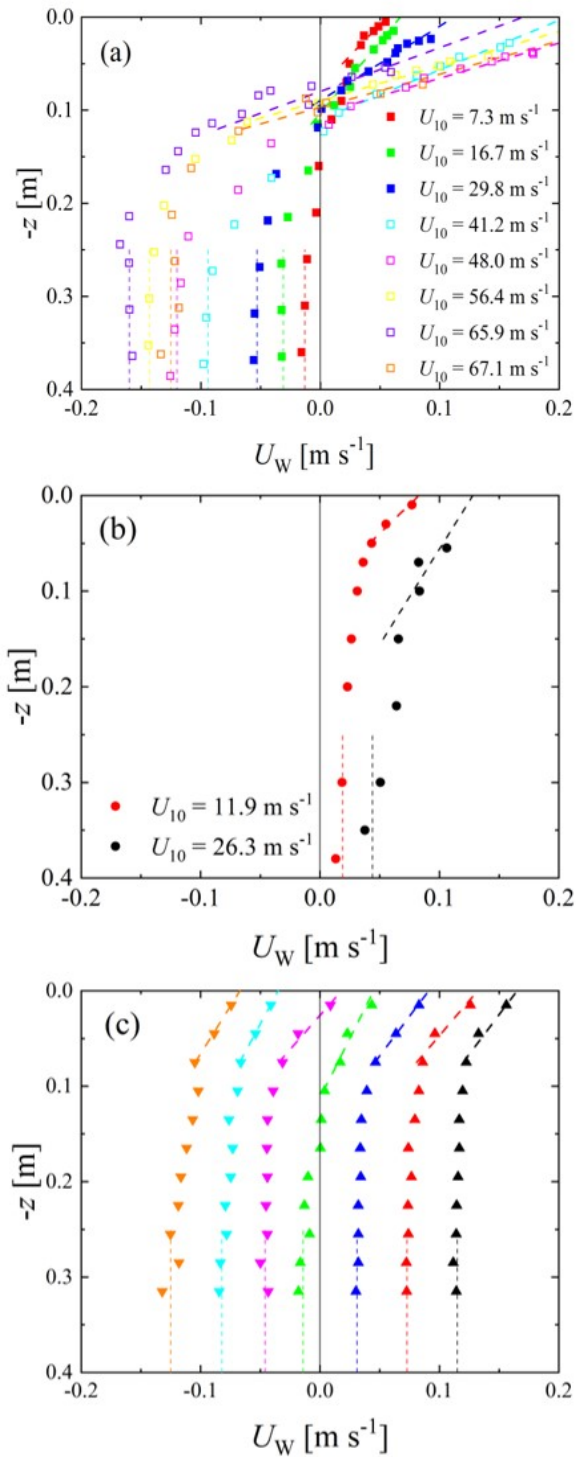
155

### 156 **3. Results and discussion**

#### 157 **3.1. Waves and current**

158 Figure 2 shows the vertical distributions of the streamwise water velocity. The  
159 water velocities in the three different wind-wave tanks at Kyoto University, Kindai  
160 University, and IAP RAS are separately shown in each subfigure. In Fig. 2a, the bulk  
161 velocity of water  $U_{\text{BULK}}$  shows negative values ( $U_{\text{BULK}} = -0.16$  to  $-0.01$  m s<sup>-1</sup>) at Kyoto  
162 University, which is generated as the counterflow against the Stokes drift at the wavy  
163 water surface. In Fig. 2b, the bulk velocity of water demonstrates positive values ( $U_{\text{BULK}}$   
164  $= 0.019$  to  $0.044$  m/s) at IAP RAS, because the wind-wave flume is submerged; thus, the  
165 Stokes drift on the wavy water surface does not provide the counterflow for the bulk  
166 water, unlike in the closed tank at Kyoto University. From Fig. 2c, it is clear that the bulk  
167 velocities of the water vary in each case at Kindai University with the use of the pump.  
168 Furthermore, the water bulk velocities change from negative to positive ( $U_{\text{BULK}} = -0.13$   
169 to  $-0.17$  m s<sup>-1</sup>). The bulk velocities of water were defined as the mean velocity with  $z =$   
170  $-0.4$  to  $-0.25$  m (see dotted lines in Fig. 2), and the velocities are listed in Table 1.  
171 Experiments were performed under 27 different conditions, with the bulk velocity of  
172 water provided in the three different wind-wave tanks. The surface velocities of water,  
173  $U_{\text{SURF}}$ , also varied in the three tanks with respect to wind speed (see Fig. 2). The  $U_{\text{SURF}}$   
174 values were estimated by the linear extrapolation lines (dashed lines) as the water velocity  
175 at the surface ( $z = 0$  m) shown in Fig. 2, and the velocities are listed in Table 1.

176 Figure 3 shows the wind-velocity dependency of the wave frequency  $f_m$ ,  
177 wavelength  $L_S$ , phase velocity  $C_S$ , surface velocity of water  $U_{\text{SURF}}$ , and bulk velocity of  
178 water  $U_{\text{BULK}}$ . From Figs. 3a–3c, it is clear that both the Kyoto and IAP RAS data  
179 demonstrate that the wind waves develop with wind shear. Although  $f_m$  in both cases  
180 correspond to each other,  $L_S$  and  $C_S$  in IAP RAS are different from those in Kyoto. The  
181 disagreement might be caused by the difference in the wind-wave development or  
182 Doppler effect; this is discussed below. From Figs. 3d and 3e,  $U_{\text{SURF}}$  and  $U_{\text{BULK}}$  increase  
183 with an increase in  $U_{10}$  in IAP RAS. However, in Kyoto,  $U_{\text{SURF}}$  increases, but  $U_{\text{BULK}}$   
184 decreases with an increase in  $U_{10}$ . Moreover,  $U_{\text{SURF}}$  in IAP RAS corresponds to  $U_{\text{SURF}}$  in  
185 Kyoto. This is because the Stokes drift generated by the wind waves, rather than the  
186 current, is significant. For the Kindai data, although  $f_m$ ,  $U_{\text{SURF}}$ , and  $U_{\text{BULK}}$  vary,  $L_S$  and  $C_S$   
187 are concentrated at single points at  $L_S = 0.1$  m and  $C_S = 0.4$  m s<sup>-1</sup>, respectively.



188

189 **Figure 2.** Vertical distributions of water-flow velocity; (a) Kyoto University, (b) IAP RAS, and (c)

190 Kindai University. In (c), plots indicate cases 21–27 starting from right. Dotted and dashed lines

191 indicate the lines used to estimate  $U_{BULK}$  and  $U_{SURF}$ , respectively. Open symbols show the

192 high-wind-speed cases.

193 **TABLE 1.** Wind and wind-wave properties.  $F$ : fetch;  $N_{\text{PUMP}}$ : pump inverter frequency;  $U_{\infty}$ :  
194 freestream wind speed;  $u^*$ : friction velocity of air;  $U_{10}$ : wind speed at 10 m above the sea surface;  
195  $U_{\text{SURF}}$ : surface flow velocity of water;  $U_{\text{BULK}}$ : bulk flow velocity of water;  $C_D$ : drag coefficient;  $H_s$ :  
196 significant wave height;  $T_s$ : significant wave period;  $E$ : wave energy;  $f_m$ : significant frequency;  $C_s$ :  
197 phase velocity;  $L_s$ : significant wave length;  $C_{s\text{-theor-l}}$ : phase velocity predicted by theoretical linear  
198 model;  $C_{s\text{-theor-nl}}$ : phase velocity predicted by theoretical nonlinear model. The values of  $u^*$ ,  $U_{10}$ , and  
199  $C_D$  in Kindai were estimated using the empirical curves by Iwano et al. (2013) from  $U_{\infty}$ . Superscripts  $\dagger$   
200 and  $\dagger\dagger$  indicate the artificial following and opposing flows, respectively.

Case	Facility	$F$	$N_{\text{pump}}$	$U_{\infty}$	$u^*$	$U_{10}$	$U_{\text{SURF}}$	$U_{\text{BULK}}$	$C_D$	$H_s$	$T_s$	$E^{0.5}$	$f_m$	$C_s$	$L_s$	$C_{s\text{-theor-l}}$	$C_{s\text{-theor-nl}}$
		[m]	[Hz]	[m s <sup>-1</sup> ]	[m s <sup>-1</sup> ]	[m s <sup>-1</sup> ]	[m s <sup>-1</sup> ]	[m s <sup>-1</sup> ]	[ $\times 10^{-3}$ ]	[m]	[m]	[m]	[Hz]	[m s <sup>-1</sup> ]	[m]	[m s <sup>-1</sup> ]	[m s <sup>-1</sup> ]
1	Kyoto	6.5	-	4.7	0.24	7.3	0.056	-0.01	1.1	0.0035	0.15	0.00092	6.63	0.40	0.06	0.369	0.374
2	Kyoto	6.5	-	7.2	0.43	11.5	-	-	1.4	0.0131	0.25	0.00353	3.95	0.59	0.16	-	-
3	Kyoto	6.5	-	10.3	0.67	16.7	0.067	-0.031	1.6	0.0231	0.32	0.00624	3.03	0.69	0.23	0.658	0.690
4	Kyoto	6.5	-	12.6	0.89	21.5	-	-	1.7	0.0357	0.39	0.00968	2.59	0.92	0.38	-	-
5	Kyoto	6.5	-	16.3	1.49	29.8	0.112	-0.053	2.5	0.0584	0.50	0.01570	2.01	1.09	0.52	0.972	1.044
6	Kyoto	6.5	-	18.8	1.70	33.6	-	-	2.5	0.0626	0.52	0.01691	1.89	1.18	0.60	-	-
7	Kyoto	6.5	-	22.2	2.08	41.2	0.206	-0.094	2.6	0.0631	0.53	0.01735	1.86	1.35	0.74	1.188	1.258
8	Kyoto	6.5	-	24.8	-	-	-	-	-	0.0668	0.55	0.01866	1.76	1.41	0.79	-	-
9	Kyoto	6.5	-	28.5	2.36	48.0	0.273	-0.120	2.4	0.0727	0.58	0.02058	1.68	1.54	0.93	1.325	1.424
10	Kyoto	6.5	-	31.1	-	-	-	-	-	0.0807	0.62	0.02309	1.58	1.60	1.07	-	-
11	Kyoto	6.5	-	34.8	2.69	56.4	0.241	-0.143	2.3	0.0944	0.68	0.02715	1.44	1.64	1.10	1.379	1.550
12	Kyoto	6.5	-	37.1	2.89	57.7	-	-	2.5	0.1043	0.73	0.03027	1.37	1.76	1.31	-	-
13	Kyoto	6.5	-	39.6	3.38	65.9	0.170	-0.160	2.6	0.1214	0.80	0.03553	1.20	1.84	1.51	1.531	1.694
14	Kyoto	6.5	-	43.3	3.31	67.1	0.272	-0.125	2.4	0.1609	0.93	0.04766	1.08	2.01	1.92	1.743	2.149
15	IAP RAS	6.5	-	8.5	0.40	11.9	0.083	0.019	1.1	0.0214	0.31	0.0056	3.14	0.78	0.25	0.690	0.715
16	IAP RAS	6.5	-	11.0	0.60	16.7	-	-	1.3	0.0305	0.36	0.0081	2.84	0.89	0.32	-	-
17	IAP RAS	6.5	-	13.5	0.90	21.9	-	-	1.7	0.0455	0.43	0.0121	2.41	1.07	0.45	-	-
18	IAP RAS	6.5	-	16.3	1.15	26.3	0.128	0.044	1.9	0.0790	0.50	0.0161	1.95	1.27	0.65	1.111	1.190
19	IAP RAS	6.5	-	18.9	1.50	32.5	-	-	2.1	0.0690	0.54	0.0246	1.85	1.37	0.74	-	-
20	IAP RAS	6.5	-	21.2	1.70	36.9	-	-	2.1	0.0847	0.60	0.0305	1.61	1.61	1.00	-	-
21	Kindai	4.0	15 <sup>†</sup>	5.8	0.28	7.9	0.165	0.115	1.2	0.0044	0.14	0.0012	6.92	0.43	0.06	0.484	0.492
22	Kindai	4.0	10 <sup>†</sup>	5.8	0.28	7.9	0.132	0.073	1.2	0.0050	0.16	0.0014	6.10	0.43	0.07	0.501	0.510
23	Kindai	4.0	5 <sup>†</sup>	5.8	0.28	7.9	0.091	0.031	1.2	0.0049	0.16	0.0014	6.16	0.38	0.06	0.410	0.420
24	Kindai	4.0	0	5.8	0.28	7.9	0.045	-0.014	1.2	0.0054	0.19	0.0014	5.47	0.38	0.07	0.382	0.393
25	Kindai	4.0	5 <sup>††</sup>	5.8	0.28	7.9	0.018	-0.046	1.2	0.0076	0.23	0.0021	4.25	0.36	0.08	0.384	0.400
26	Kindai	4.0	10 <sup>††</sup>	5.8	0.28	7.9	-0.035	-0.082	1.2	0.0098	0.27	0.0027	3.64	0.35	0.10	0.355	0.375
27	Kindai	4.0	15 <sup>††</sup>	5.8	0.28	7.9	-0.067	-0.125	1.2	0.0125	0.34	0.0035	2.94	0.38	0.13	0.381	0.402

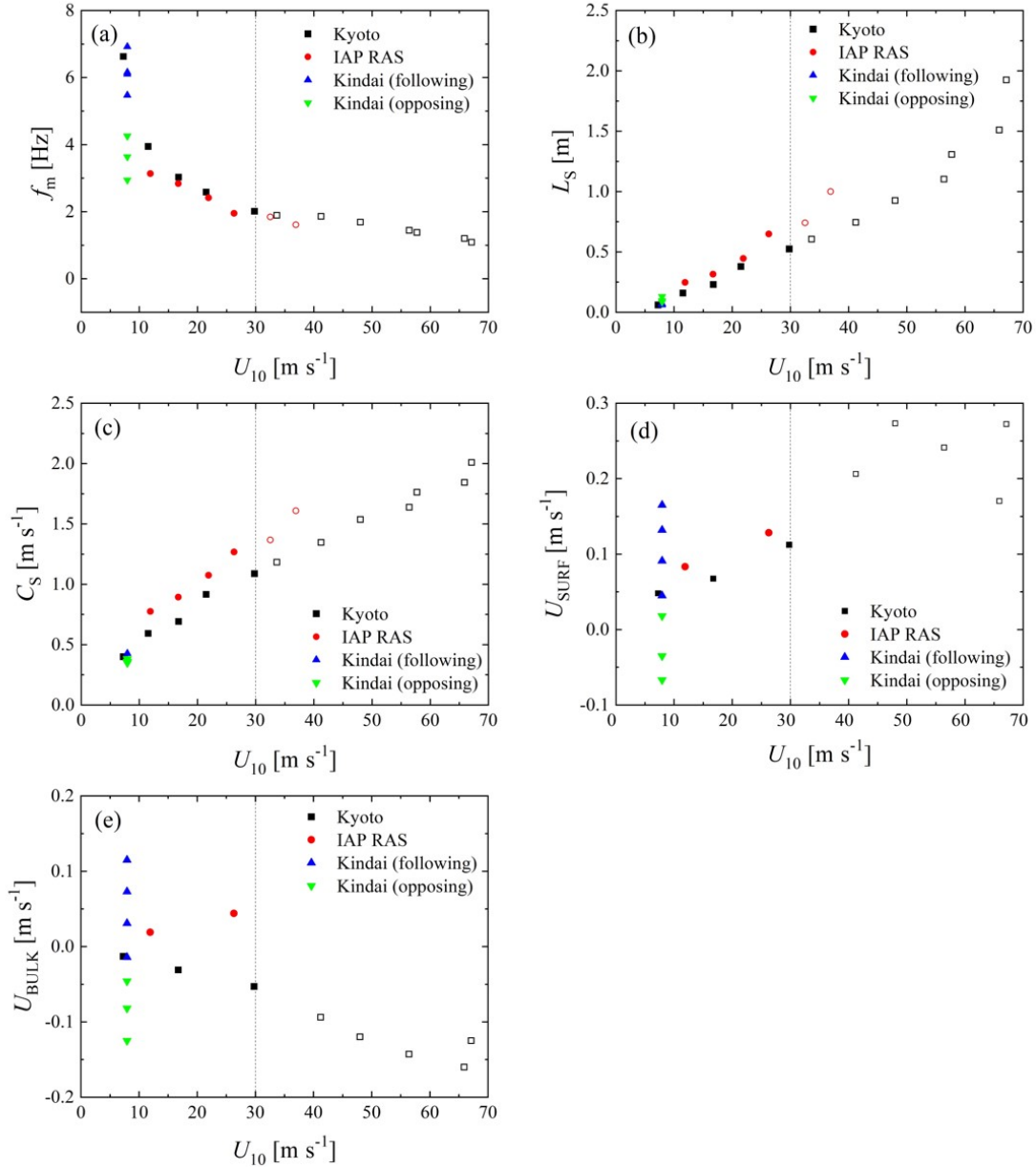
201

202

203 This shows that the intensity and direction of the current do not significantly affect  $L_s$  and  
204  $C_s$  but do affect  $f_m$  and  $U_{\text{SURF}}$ . Thus, this implies that the present artificial current changes  
205 the water flow dramatically but does not affect the development of the wind waves.

206 Figure 4 shows the dispersion relation and demonstrates that the Kindai data  
207 points depend on the variation in the water velocity of the artificial current. The plots for  
208 the Kyoto University and IAP RAS cases at normal wind speeds (solid symbols) are  
209 concentrated above the solid curve, showing the dispersion relation of the deep-water



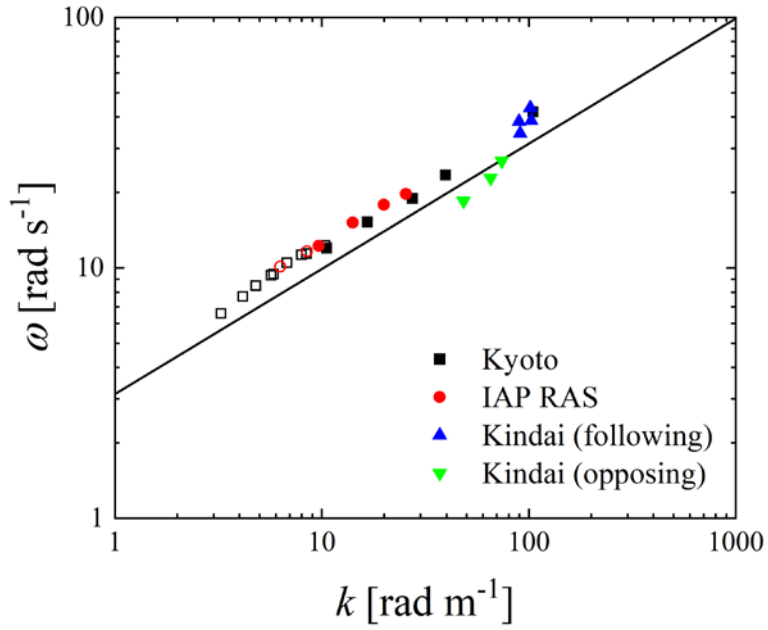


210

211 **Figure 3.** Relationships between  $U_{10}$  and (a) significant frequency  $f_m$ , (b) significant wave length  $L_s$ ,  
 212 (c) phase velocity  $C_s$ , (d) surface velocity of water  $U_{SURF}$ , and (e) bulk velocity of water  $U_{BULK}$ . Open  
 213 symbols show the high-wind-speed cases.

214

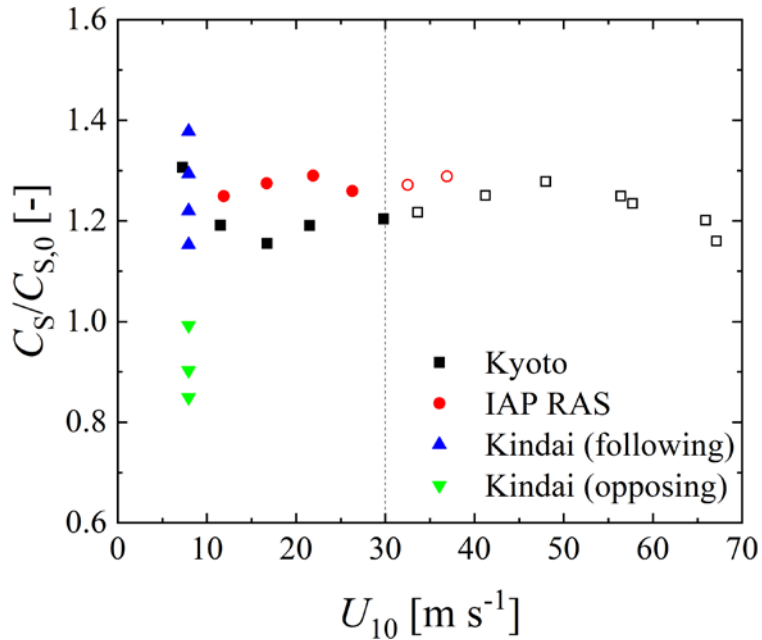
215 waves ( $\omega^2 = gk$ ). Meanwhile, the plots for extreme high wind speeds (open symbols) are  
 216 also concentrated above the solid curve. This implies that the wind waves, along with the  
 217 intensive breaking at extreme high wind speeds, are dependent on the Doppler shift. To  
 218 investigate the phase velocity trend, Fig. 5 shows the ratio of the measured phase velocity



219

220 **Figure 4.** Dispersion relation between angular frequency  $\omega$  and wave number  $k$ . Open symbols show  
 221 the high-wind-speed cases. Curve shows the dispersion relation of the deep-water waves ( $\omega^2 = gk$ ).

222



223

224 **Figure 5.** Relationship between the freestream wind speed and phase velocity  $C_s$ . The  $C_s$  is  
 225 normalized by phase velocity  $C_{s,0}$  without the Doppler effect, estimated by the dispersion relation of  
 226 the deep-water waves ( $C_{s,0} = (gL_s/2\pi)^{1/2}$ ). Open symbols show the high-wind-speed cases.

227  $C_S$  to the phase velocity  $C_{S,0}$  estimated by the dispersion relation of the deep-water waves  
228 ( $C_{S,0} = (gL_S/2\pi)^{1/2}$ ) against the wind velocity. From the figure, the ratios at the normal  
229 wind speeds assume a constant value ( $\sim 1.21$  in Kyoto or  $\sim 1.27$  in IAP RAS). Moreover,  
230 the ratios at the extreme high wind speeds take similar values of 1.23 and 1.28 for Kyoto  
231 or IAP RAS, respectively. This implies that the phase velocities at extreme high wind  
232 speeds are accelerated by the current just as those at normal wind speeds. However, the  
233 Kindai values are scattered and increase in the following cases and decrease in the  
234 opposing cases. It is clear that the artificial current accelerates (or decelerates) the phase  
235 velocity.

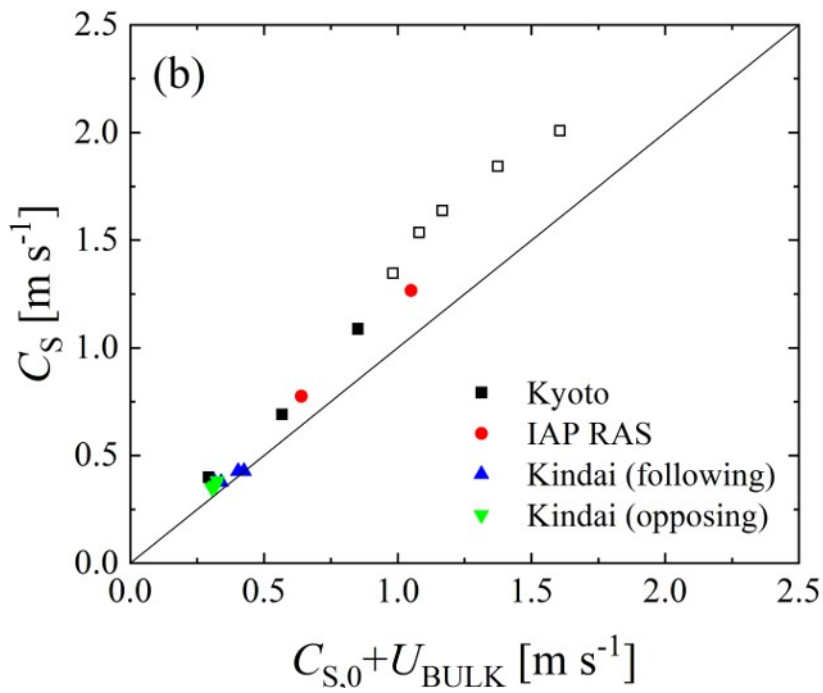
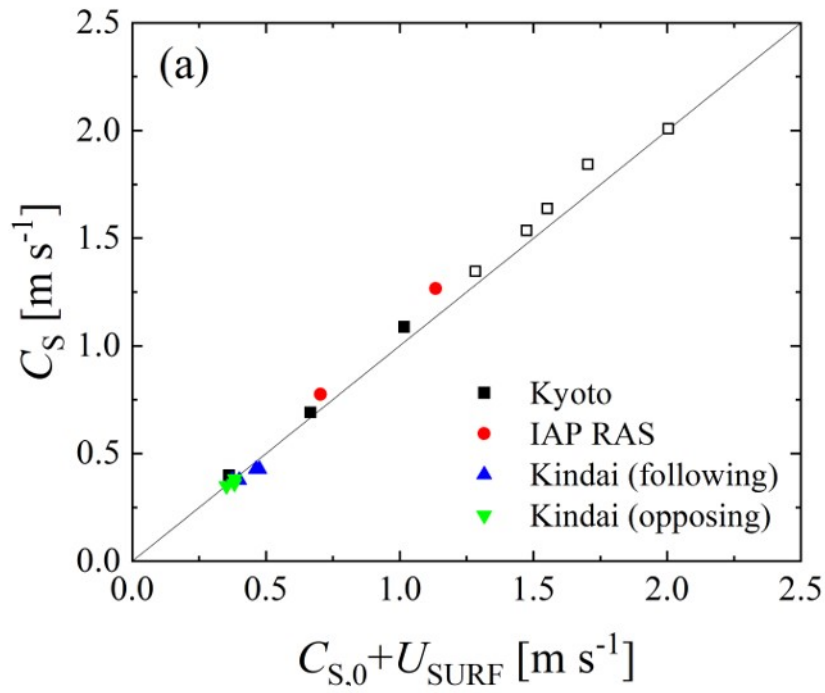
236 To interpret the relationship among the measured phase velocity  $C_S$ , first phase  
237 velocity  $C_{S,0}$  estimated by the dispersion relation, and water velocity, two types of phase  
238 velocity were evaluated: the sum of  $C_{S,0}$  and surface velocity of water  $U_{SURF}$  and the sum  
239 of  $C_{S,0}$  and bulk velocity of water  $U_{BULK}$ . Figure 6 shows the relationship between  $C_S$  and  
240 (a)  $C_{S,0} + U_{SURF}$ , and (b)  $C_{S,0} + U_{BULK}$ . In Fig. 6a, we can see that the Doppler shift is  
241 confirmed at the normal wind speeds, i.e., the significant waves are accelerated by the  
242 surface flow, and the real phase velocity can be represented as the sum of the velocity of  
243 the surface flow and the virtual phase velocity, which is estimated by the dispersion  
244 relation of the deep-water waves. At extreme high wind speeds over  $30 \text{ m s}^{-1}$ , a similar  
245 Doppler shift is observed as under the conditions of normal wind speeds, as seen in Fig.  
246 6a. Meanwhile, in Fig. 6b, although  $C_S$  corresponds to  $C_{S,0} + U_{BULK}$  at low phase  
247 velocities,  $C_S$  assumes values larger than  $C_{S,0} + U_{BULK}$  at high phase velocities. This  
248 suggests that the Doppler shift is an adequate model for representing the acceleration of  
249 the wind waves by the current, not only for the wind waves at normal wind speeds but  
250 also for those with intensive breaking at extreme high wind speeds. Moreover, the  
251 Doppler shift of wind waves occurs due to a very thin surface flow, as the correlation  
252 between  $C_S$  and  $C_{S,0} + U_{SURF}$  is higher than the correlation between  $C_S$  and  $C_{S,0} + U_{BULK}$ .

253

### 254 **3.2. The theoretical model of waves at the shear flow**

255 The parameters of the observed Doppler shift can be explained more precisely  
256 within the theoretical model of the capillary-gravity waves at the surface of the water  
257 flows with the velocity profiles prescribed by the experimental data, which are plotted in  
258 Fig. 2a–c. Because the dominant wind wave propagates along the wave and water flows,  
259 we will consider the 2D-wave model in the 2D flow. This flow is described by the system  
260 of 2D Euler equations:

261



262

263 **Figure 6.** Relationship between phase velocity  $C_S$  and (a) sum of  $C_{S,0}$  and surface velocity of water  
 264  $U_{\text{SURF}}$ , and (b) sum of  $C_{S,0}$  and bulk velocity of water  $U_{\text{BULK}}$ . Open symbols show the high-wind-speed  
 265 cases.

266

267 
$$\frac{\partial u}{\partial t} + u \frac{\partial u}{\partial x} + w \frac{\partial u}{\partial z} + \frac{1}{\rho} \frac{\partial p}{\partial x} = 0, \quad (3)$$

268 
$$\frac{\partial w}{\partial t} + u \frac{\partial w}{\partial x} + w \frac{\partial w}{\partial z} + \frac{1}{\rho} \frac{\partial p}{\partial z} = -g,$$

269 and the condition of non-compressibility:

270 
$$\frac{\partial u}{\partial x} + \frac{\partial w}{\partial z} = 0, \quad (4)$$

271 with the kinematical

272 
$$\frac{\partial \eta}{\partial t} + u \frac{\partial \eta}{\partial x} = w \Big|_{z=\eta(x,t)} \quad (5)$$

273 and dynamical boundary conditions

274 
$$p \Big|_{z=\eta(x,t)} = 0 \quad (6)$$

275 at the water surface. Here,  $u$  and  $w$  are the horizontal and vertical velocity components,  $p$   
 276 is the water pressure,  $x$  and  $z$  are the horizontal and upward vertical coordinates,  $g$  is the  
 277 gravity acceleration, and  $\rho$  is the water density. The boundary condition at the bottom of  
 278 the channel is  $w \Big|_{z=-D} = 0$ . It should be noted that the water depth in almost all the  
 279 experimental runs exceeded half of the wavelength of the dominant waves (see Table 1).  
 280 In this case, the deep-water approximation is applicable for describing the surface waves,  
 281 and the boundary condition of the wave field vanishing with the distance from the water  
 282 surface can also be used.

283 Because the fluid motion under consideration is 2D, the stream function can be  
 284 introduced as follows:

285 
$$u = \frac{\partial \psi}{\partial z}; w = -\frac{\partial \psi}{\partial x}. \quad (7)$$

286 To derive the linear dispersion relation for the surface waves at the plane shear flow with  
 287 the horizontal velocity profile  $U_w(z)$ , we consider the solution to Eqs. (3, 4) in terms of the  
 288 stream function as the sum of the undisturbed state with steady shear flow and  
 289 small-amplitude disturbances. Then, the stream function  $\psi$  and pressure  $p$  are as follows:

290 
$$\psi(x, z, t) = \int_{z_1}^z U_w(z_1) dz_1 + \varepsilon \psi_1(x, z, t); \quad (8)$$

291 
$$p(x, z, t) = -\rho g z + \varepsilon p_1(x, z, t), \quad (9)$$

292 where  $\varepsilon \ll 1$ , and the water elevation value is also the order of  $\varepsilon$ , namely  $\varepsilon\eta_1(x, t)$ .

293 In the linear approximation in  $\varepsilon$ , the system of Eqs. (3, 4) and the boundary  
294 conditions of Eqs. (5, 6) take the form:

$$295 \left( \frac{\partial}{\partial t} + \frac{U_w(z)\partial}{\partial x} \right) \left( \frac{\partial^2 \psi_1}{\partial x^2} + \frac{\partial^2 \psi_1}{\partial z^2} \right) - \frac{\partial \psi_1}{\partial x} \frac{d^2 U_w(z)}{dz^2} = 0,$$

$$296 \frac{\partial \eta_1}{\partial t} + U_w(0) \frac{\partial \eta_1}{\partial x} = - \frac{\partial \psi_1}{\partial x} \Big|_{z=0}, \quad (10)$$

$$297 \frac{\partial p_1}{\partial x} \Big|_{z=0} - \rho g \frac{\partial \eta_1}{\partial x} = 0,$$

$$298 \psi_1 \Big|_{z=-D} = 0.$$

299 Excluding  $p_1$  with use of the first equation of the system in Eq. (3) and eliminating  $\eta_1$   
300 yields one boundary condition at the water surface for  $\psi_1$ :

$$301 \left[ \left( \frac{\partial}{\partial t} + \frac{U_w(0)\partial}{\partial x} \right)^2 \frac{\partial \psi_1}{\partial z} - \left( \frac{\partial}{\partial t} + U_w(0) \frac{\partial}{\partial x} \right) \frac{\partial \psi_1}{\partial x} \frac{dU_w}{dz} - g \frac{\partial^2 \psi_1}{\partial x^2} \right] \Big|_{z=0} = 0. \quad (11)$$

302 For the harmonic wave disturbance, where

$$303 \psi_1(x, z, t) = \Psi(t) \exp(-i(\omega t - kt)), \quad (12)$$

304 substituting into Eqs. (10, 11) yields the Rayleigh equation for the complex amplitude of  
305 the stream function disturbance:

$$306 (\omega - U_w(z)k) \left( \frac{d^2 \Psi_1}{dz^2} - k^2 \Psi_1 \right) + \frac{d^2 U_w(z)}{dz^2} k^2 \Psi_1 = 0, \quad (13)$$

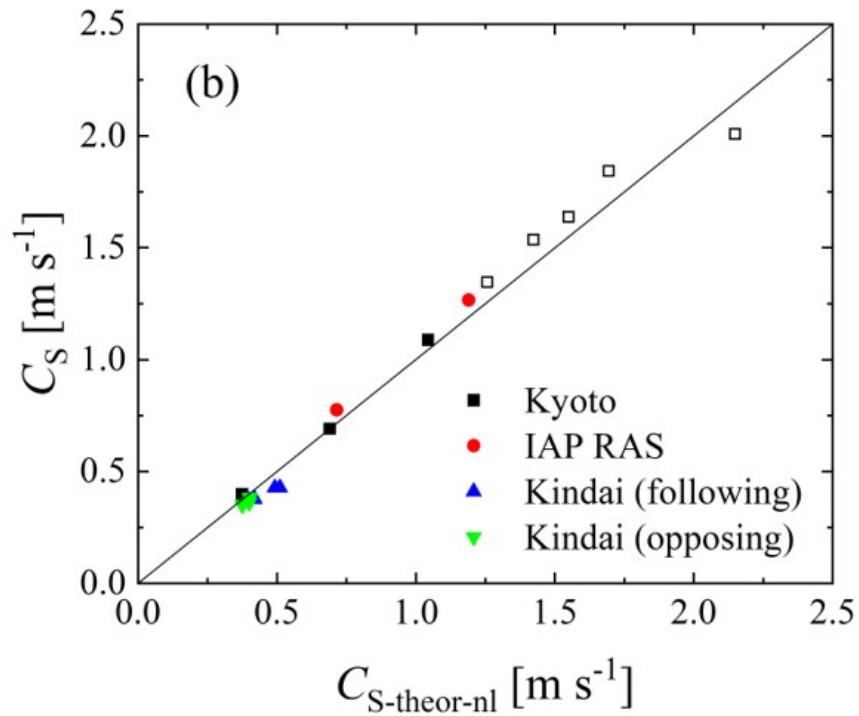
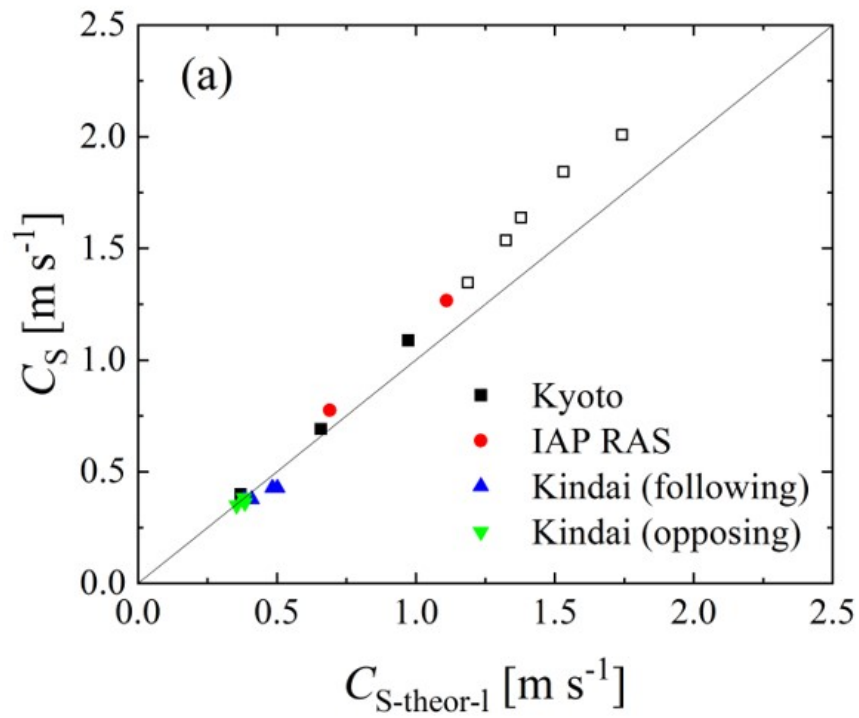
307 with the following boundary condition:

$$308 (\omega - U_w(0)k)^2 \frac{d\Psi_1(0)}{dz} + (\omega - U_w(0)k)k\Psi_1(0) \frac{dU_w(0)}{dz} - k^2 g\Psi_1(0) = 0, \quad (14)$$

$$309 \Psi_1 \Big|_{z \rightarrow -\infty} \rightarrow 0.$$

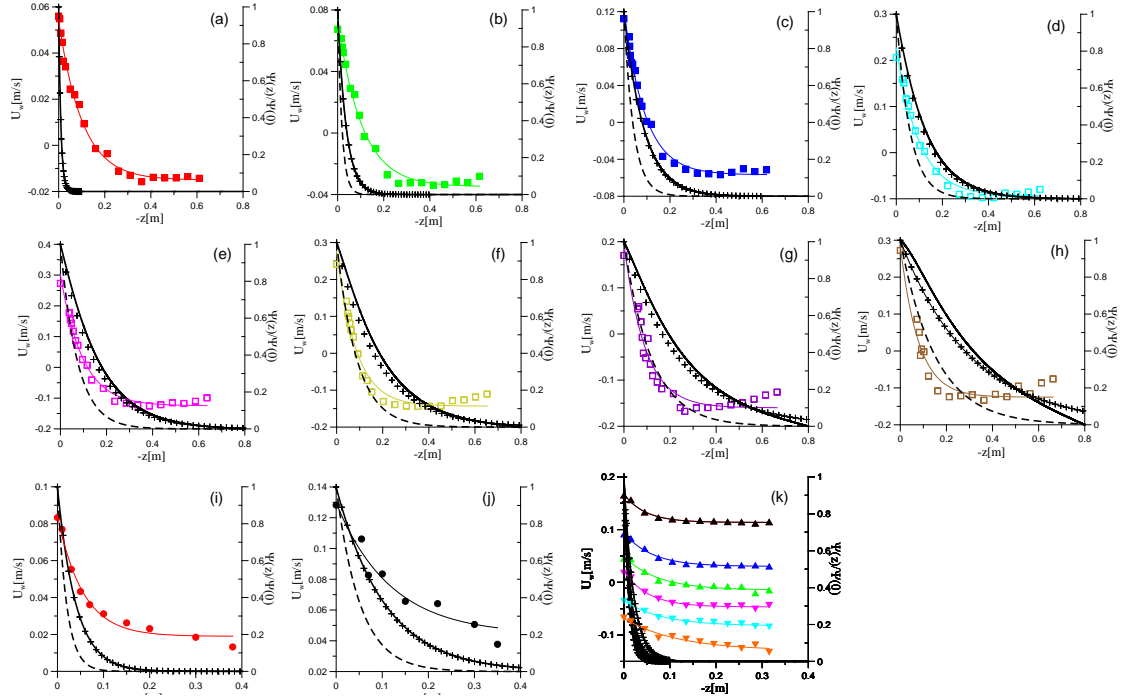
310 Numerically solving the boundary layer problem for Eq. (13) with the boundary  
311 conditions in Eq. (14) enables one to obtain the dispersion relation  $\omega(k)$  for the surface  
312 waves at the inhomogeneous shear flow. Note that because the phase velocity of the  
313 waves significantly exceeded the flow velocity in all experiments (cf. Figs. 2 and 3), the  
314 Rayleigh equation did not have a singularity, and the calculated frequency and phase  
315 velocity of the wave were real values, i.e., the current was neutral stable.

316 The wave phase velocities  $C_{S\text{-theor-1}} = \omega(k)/k$  were calculated for the parameters of  
317 those experiments that contained complete information about the course and  
318 characteristics of the waves, namely 1, 3, 5, 7, 9, 11, 13–15, 18, and 21–27 from Table 1.  
319 The results are presented in Fig. 7a as the measured phase velocity  $C_s$  versus calculated



320  
321  
322  
323

**Figure 7.** The measured phase velocity  $C_S$  versus theoretical prediction: (a) linear model, and (b) nonlinear model.



324

325 **Figure 8.** Vertical velocity profiles (points), their fitting (thin color line), the eigenfunction of the Eq.  
 326 (8) with the boundary conditions Eq. (9) (black solid curve), the function  $e^{kz}$  (crosses), the function  $e^{2kz}$   
 327 (dashed line). The panels (a)-(j) corresponds to the experiments No. 1, 3, 5, 7, 9, 11, 13-15, 18  
 328 respectively, the panel (k) corresponds to the experiments No. 21-27.

329

330 phase velocity  $C_{S\text{-theor-1}}$ . One can see that the model corresponds to the data substantially  
 331 better than does the model of linear potential waves at the homogeneous current  $U_{\text{BULK}}$   
 332 (compare Fig. 6b). Considering the structure of the wave disturbances of the stream  
 333 function,  $\Psi_1(z)$ , which was found as the eigenfunction of the boundary problem of Eqs.  
 334 (11, 12). The profiles of  $\Psi_1(z)$  are presented in Fig. 8. One can see that in all cases the  
 335 functions  $\Psi_1(z)$  are close to  $e^{kz}$  at the background of the mean velocity profiles. Moreover,  
 336 for experiments No. 1, 3, 5, 15, and 21–27 (see Fig. 8a, 8b, 8c, 8i, and 8k), the wave field  
 337 is concentrated near the surface at a distance less than the scale of the change in the mean  
 338 flow, where the flow velocity is approximately equal to  $U_{\text{SURF}}$ . This explains the good  
 339 correlation in these cases of the observed phase velocity with the phase velocity of waves  
 340 at the homogeneous current  $U_{\text{SURF}}$  presented in Fig. 6a. At the same time, for experiments  
 341 No. 7, 9, 5, 11, 13, 14, and 18 (see Figs. 8d–8h, and 8j), the scale of the variability of the  
 342 flow is significantly smaller than the scale of the wave field. Under these conditions, a  
 343 significant difference between the phase velocity of the waves and that given by the linear  
 344 dispersion relation can be due to the influence of nonlinearity.

345

To estimate the nonlinear addition to the wave phase velocity, we used the results



346 of the weakly nonlinear theory of surface waves for the current with a constant shear. Of  
 347 course, the flow in the experiments of the present work does not have a constant shift, and  
 348 this was considered when obtaining the linear dispersion relation. However, it should be  
 349 taken into account that the contributions of the  $n$ -th harmonic to the nonlinear dispersion  
 350 relation are determined by wave fields in the  $n$ -power, which have a scale that is  $n$  time  
 351 smaller than the first harmonic. Additionally, the model of constant shear of the mean  
 352 current velocity is already approximately applicable for the 2nd harmonic (see Fig. 8).

353 We use the nonlinear dispersion relation for waves in the current with a constant  
 354 shift in the deep-water approximation, which was obtained by Simmen and Saffman  
 355 (1985):

$$\begin{aligned}
 356 \quad & (\omega - U_w(0)k)^2 \frac{d\Psi_1(0)}{dz} + (\omega - U_w(0)k)k\Psi_1(0) \frac{dU_w(0)}{dz} - k^2 g\Psi_1(0) = \gamma(ka)^2, \\
 357 \quad & \gamma = \frac{(\omega_0 - U_w(0)k)^2}{2k} \left( 1 - \frac{1}{2}\Omega^2 + \left( 1 + 2\Omega + \frac{1}{2}\Omega^2 \right)^2 \right), \quad (15) \\
 358 \quad & \Omega = \frac{1}{(\omega_0 - U_w(0)k)} \frac{dU_w(0)}{dz},
 \end{aligned}$$

359 Here,  $\omega_0$  is the solution of the linear dispersion equation. Eq. (15) is rewritten in the  
 360 notation of this work and formulated in a reference frame in which the surface of the  
 361 water has the velocity  $U_w(0)$ . Note that the linear part of Eq. (15) coincides with Eq. (14).  
 362 The results of solving Eq. (15) are presented in Fig. 7b similarly to Fig. 7a as the  
 363 measured phase velocity  $C_S$  versus calculated phase velocity  $C_{S\text{-theor-nl}} = \omega(k)/k$ , where  
 364 one can see their good agreement with each other. Thus, the wave frequency shift can be  
 365 explained by two factors, including the Doppler shift at the mean flow and the nonlinear  
 366 frequency shift, while, the latter can also be interpreted in its physical nature as the wave  
 367 frequency shift in the presence of its orbital velocities.

368 Recent studies have indicated a regime shift in the momentum, heat, and mass  
 369 transfer across an intensive broken wave surface along with the amount of dispersed  
 370 droplets and entrained bubbles at extreme high wind speeds over  $30 \text{ m s}^{-1}$  (e.g., Powell et  
 371 al., 2003; Donelan et al., 2004; Takagaki et al., 2012, 2016; Troitskaya et al., 2012; Iwano  
 372 et al., 2013; Krall and Jähne, 2014; Komori et al., 2018; Krall et al., 2019). Thus, there is  
 373 the possibility of a similar regime shift in the Doppler shift of wind waves by the current  
 374 at extreme high wind speeds. However, the present study reveals that such a Doppler shift  
 375 is observed as under the conditions of normal wind speeds. In this case, the weakly  
 376 nonlinear approximation turns out to be applicable for describing the dispersion  
 377 properties of not only small-amplitude waves but also nonlinear and even breaking waves.  
 378 This implies that the intensive wave breaking at extreme high wind speeds occurs with

379 the saturation (or dumping) of the wave height rather than the wavelength. This evidence  
380 might be helpful in investigating and modelling the wind-wave development at extreme  
381 high wind speeds.

382

#### 383 **4. Conclusion**

384 The effects of the current on wind waves were investigated through laboratory  
385 experiments in three different wind-wave tanks with a pump at Kyoto University, Japan,  
386 Kindai University, Japan, and IAP RAS. The study investigated 27 cases with the  
387 measurements of winds, waves, and currents, at wind speeds ranging from 7–67 m s<sup>-1</sup>. We  
388 observed that the wind waves do not follow the dispersion relation in either the normal or  
389 the extremely high wind speeds in the three tanks (Fig. 4)—excluding case 25, in which  
390 the artificial current experiment used the Kindai tank. In case 25,  $U_{\text{SURF}}$  is approximately  
391 zero (Fig. 3); thus, the Doppler shift does not occur. Then, using 18 datasets (Kyoto and  
392 IAP RAS tanks) (Fig. 5), we found that the ratio of  $C_s/C_{s,0}$  is constant at both normal and  
393 extremely high wind speeds. Moreover, in the artificial current experiment in Kindai, we  
394 observed that the ratio varies (Fig. 5). The evidence from the three tank experiments  
395 implies that the same wave-current interaction occurs at normal and extremely high wind  
396 speeds.

397 To develop an adequate model for wave-current interaction at normal and  
398 extremely high wind speeds, we validated four models (Figs. 6 and 7). At normal wind  
399 speeds under 30 m s<sup>-1</sup>, the wave frequency, wavelength, phase velocity of waves, and  
400 surface velocity of the water depended on the wind speed (Fig. 3). However, the bulk  
401 velocity of the water showed a dependence on the tank type, i.e., a large tank with a  
402 submerged wind-wave flume (IAP RAS) or wind flume above a tank (general type of  
403 wind-wave tank) (Kyoto University) (Fig. 3). The effect of the Doppler shift was  
404 confirmed at normal wind speeds, i.e., the significant waves were accelerated by the  
405 surface flow, and the phase velocity was represented as the sum of the surface velocity of  
406 water and the phase velocity, which is estimated by the dispersion relation of the  
407 deep-water waves (Fig. 6). At extreme high wind speeds over 30 m s<sup>-1</sup>, a Doppler shift  
408 was observed similar to that under the conditions of normal wind speeds (Figs. 4 and 5).  
409 This suggests that the Doppler shift is an adequate model for representing the acceleration  
410 of wind waves by the current, not only for the wind waves at normal wind speeds but also  
411 for those with intensive breaking at extreme high wind speeds. The data obtained by the  
412 artificial current experiments conducted at Kindai University were used to explain how  
413 the artificial current accelerates (or decelerates) the significant waves. A weakly  
414 nonlinear model of surface waves at a shear flow was developed (Fig. 7). It was shown

415 that it describes well the dispersion properties of not only small-amplitude waves but also  
416 strongly nonlinear and even breaking waves, typical for extreme wind conditions, with  
417 speeds,  $U_{10}$ , exceeding  $30 \text{ m s}^{-1}$ .

418

#### 419 **Data availability**

420 All analytical data used in this study are compiled in Table 1.

421

#### 422 **Author contributions**

423 NT and NS planned the experiments, evaluated the data, and contributed equally to  
424 writing the paper excluding Section 3.2. YT planned the Russia experiment, provided the  
425 linear and non-linear models, prepared figures in Section 3.2, and contributed to writing  
426 Section 3.2. CT prepared all figures excluding Section 3.2. NT performed the wind,  
427 current, and wave measurements in the Kyoto experiment. NT, NS, and CT performed the  
428 wind, current, and wave measurements in the Kindai experiment. AK and MV performed  
429 the wind, current, and wave measurements in the Russia experiment.

430

#### 431 **Competing interests**

432 The authors declare that they have no conflict of interest.

433

#### 434 **Acknowledgements**

435 This work was supported by the Ministry of Education, Culture, Sports, Science and  
436 Technology (Grant-in-Aid No's. 18H01284, 18K03953, and 19KK0087). This project  
437 was supported by the Japan Society for the Promotion of Science and the Russian  
438 Foundation for Basic Research (grant 18-55-50005, 19-05-00249, 20-05-00322) under  
439 the Japan-Russia Research Cooperative Program. The experiments of IAP RAS were  
440 partially supported by RSF (project 19-17-00209). We thank Prof. S. Komori and Mr.  
441 Tsuji for their help in conducting the experiments and for useful discussions. The  
442 experiments of IAP RAS were performed at the Unique Scientific Facility "Complex of  
443 Large-Scale Geophysical Facilities" (<http://www.ckp-rf.ru/usu/77738/>).

444

#### 445 **Appendix**

446 It is important to estimate the phase velocity and wavelength of the significant  
447 wind-waves using the water-level fluctuation data. Here, we explain the method, called as  
448 the cross-spectrum method. The water-level fluctuation  $\eta(x, t)$  at arbitral location  $x$  and  
449 time  $t$  is shown as the equation:

$$\eta(x, t) = \int_{-\Omega}^{\Omega} A(\omega) e^{i(\omega t - k(\omega)x)} d\omega \quad (\text{A1})$$

450 where  $\omega$  is the angular frequency,  $A(\omega)$  is the complex amplitude, and  $k(\omega)$  is the  
 451 wavenumber of waves having  $\omega$ ,  $\Omega$  is the maximum angular frequency of the surface  
 452 waves.  $F_{\eta}(\omega)$  is the Fourier transformation of  $\eta(x, t)$  when the measurement time  $t_m$  and  $\Omega$   
 453 are sufficiently large. Using the inverse Fourier transformation of  $F_{\eta}(\omega)$ ,  $\eta(x, t)$  is shown  
 454 as:  
 455

$$\eta(x, t) = \frac{1}{2\pi} \int_{-\Omega}^{\Omega} F_{\eta}(\omega) e^{i\omega t} d\omega. \quad (\text{A2})$$

456 Comparing Eqs. (A1, A2),  $F_{\eta}(\omega)$  is  $F_{\eta}(\omega) = 2\pi A(\omega) e^{-ik(\omega)x}$ . Assuming that the wind waves  
 457 change the shape little between two wave probes set upstream and downstream, we can  
 458 set the upstream and downstream water-level fluctuations  $\eta_1(t) = \eta(0, t)$  and  $\eta_2(t) = \eta(\Delta x,$   
 459  $t)$ , respectively, with  $\Delta x$  downstream from the first probe. The Fourier transformations  
 460  $F_{\eta_1}(\omega)$  and  $F_{\eta_2}(\omega)$  for  $\eta_1(t)$  and  $\eta_2(t)$ , respectively, are shown as:

$$F_{\eta_1}(\omega) = 2\pi A(\omega), \quad (\text{A3})$$

$$F_{\eta_2}(\omega) = 2\pi A(\omega) e^{-ik(\omega)\Delta x}. \quad (\text{A4})$$

461 Then, the power spectra  $S_{\eta_1\eta_1}(\omega)$  and  $S_{\eta_2\eta_2}(\omega)$  for  $\eta_1(t)$  and  $\eta_2(t)$ , respectively, are shown  
 462 as:

$$S_{\eta_1\eta_1}(\omega) = \frac{1}{t_m} F_{\eta_1}^*(\omega) F_{\eta_1}(\omega) = \frac{1}{t_m} 4\pi^2 |A(\omega)|^2, \quad (\text{A5})$$

$$S_{\eta_2\eta_2}(\omega) = \frac{1}{t_m} F_{\eta_2}^*(\omega) F_{\eta_2}(\omega) = S_{\eta_1\eta_1}(\omega). \quad (\text{A6})$$

463 Here, the superscript \* indicates the complex conjugate number. The cross-spectrum  
 464  $Cr(\omega)$  for  $\eta_1(t)$  and  $\eta_2(t)$  is shown as:

$$Cr(\omega) = \frac{1}{t_m} F_{\eta_1}^*(\omega) F_{\eta_2}(\omega) = \frac{1}{t_m} 4\pi^2 |A(\omega)|^2 e^{ik(\omega)\Delta x}. \quad (\text{A7})$$

470 Using Euler's theorem, Eq. (A7) transforms to:

$$\begin{aligned} Cr(\omega) &= \frac{1}{t_m} 4\pi^2 |A(\omega)|^2 (\cos k(\omega)\Delta x + i \sin k(\omega)\Delta x) \\ &= S_{\eta_1}(\omega) (\cos k(\omega)\Delta x + i \sin k(\omega)\Delta x). \end{aligned} \quad (\text{A8})$$

471 The cospectrum  $Co(\omega)$  and quad spectrum  $Q(\omega)$  are defined as the real and imaginary  
 472 parts of  $Cr(\omega)$ , respectively, shown as  $Cr(\omega) = Co(\omega) + iQ(\omega)$ . Moreover, the phase  $\theta(\omega)$   
 473 is defined as  $\theta(\omega) = \tan^{-1}(Q(\omega)/Co(\omega))$ . Thus,  $\theta(\omega)$  can be calculated as:

$$\theta(\omega) = \tan^{-1}(\tan(k(\omega)\Delta x)) = k(\omega)\Delta x. \quad (\text{A9})$$

474 Generally, the velocity of the wind waves  $C$  is defined as:

$$C = \frac{\omega}{k} = \frac{L}{T}, \quad (\text{A10})$$

479 where  $L$  is the wavelength and  $T$  is the wave period. From Eqs. (A9, A10),  $C(\omega)$  and  $L(\omega)$   
 480 can be transformed to  
 481

$$C(\omega) = \frac{\omega}{k} = \frac{\omega \Delta x}{\theta(\omega)}, \quad (\text{A11})$$

482

$$L(\omega) = \frac{2\pi}{k} = \frac{2\pi \Delta x}{\theta(\omega)}. \quad (\text{A12})$$

483

484 When we estimate the phase  $\theta_m(\omega_m)$  at the angular frequency of significant wind-waves  
 485  $\omega_m (=2\pi f_m)$ , the phase velocity of the significant wind waves  $C_s (= C(\omega_m))$  and significant  
 486 wavelength  $L_s (= L(\omega_m))$  are calculated by:

$$C_s = \frac{2\pi f_m \Delta x}{\theta(f_m)}, \quad (\text{A13})$$

487

$$L_s = \frac{2\pi \Delta x}{\theta(f_m)}. \quad (\text{A14})$$

488

489 In the study,  $C_s$  and  $L_s$  are estimated by Eqs. (A13, A14) using the cross-spectrum  
 490 method.

491

492

493

### References

- 494 Dawe, J. T., Thompson, L., (2006), Effect of ocean surface currents on wind stress, heat  
 495 flux, and wind power input to the ocean, *Geophysical Research Letters*, 33, L09604,  
 496 doi:10.1029/2006GL025784
- 497 Donelan, M.A., Haus, B.K., Reul, N., Plant, W.J., Stiassnie, M., Graber, H.C., Brown,  
 498 O.B., Saltzman, E.S., (2004), On the limiting aerodynamic roughness of the ocean  
 499 in very strong winds, *Geophysical Research Letters*, 31,  
 500 doi:10.1029/2004GL019460. L18306
- 501 Fan, Y., Ginis, I., Hara, T., (2009), The Effect of Wind–Wave–Current Interaction on  
 502 Air–Sea Momentum Fluxes and Ocean Response in Tropical Cyclones, *Journal of*  
 503 *Physical Oceanography*, 39, pp. 1019-1034.
- 504 Iwano, K., Takagaki, N., Kurose, R., Komori, S., (2013), Mass transfer velocity across  
 505 the breaking air-water interface at extremely high wind speeds, *Tellus B* 65, 21341,  
 506 doi:10.3402/tellusb.v65i0.21341

507 Kara, A. B., Metzger, E. J., Bourassa, M. A., (2007), Ocean current and wave effects on  
508 wind stress drag coefficient over the global ocean, *Geophysical Research Letters*,  
509 34, L01604, doi:10.1029/2006GL027849

510 Kawabe, M., (1988), Variability of Kuroshio velocity assessed from the sea-level  
511 difference between Naze and Nishinoomote, *Journal of oceanographical Society of*  
512 *Japan*, 44, pp. 293-304.

513 Kelly, K. A., Dickinson, S., McPhaden, M. J., Johnson, G. C., (2001), Ocean currents  
514 evident in satellite wind data, *Geophysical Research Letters*, 28(12), pp.  
515 2469-2472.

516 Komori, S., Iwano, K., Takagaki, N., Onishi, R., Kurose, R., Takahashi, K., Suzuki, N.,  
517 (2018), Laboratory measurements of heat transfer and drag coefficients at  
518 extremely high wind speeds, *Journal of Physical Oceanography*,  
519 doi:10.1175/JPO-D-17-0243.1

520 Krall, K. E., Jähne, B., (2014), First laboratory study of air-sea gas exchange at hurricane  
521 wind speeds, *Ocean Science*, 10(2), 257-265, doi:10.5194/os-10-257-2014

522 Krall, K. E., Smith, A. W., Takagaki, N., Jähne, B., (2019), Air-sea gas exchange at wind  
523 speeds up to 85 m s<sup>-1</sup>, *Ocean Science*, 15(6), doi: 10.5194/os-15-1783-2019

524 Powell, M. D., Vickery, P. J., Reinhold, T. A., (2003), Reduced drag coefficient for high  
525 wind speeds in tropical cyclones, *Nature*, 422, 279–283, doi:10.1038/nature01481

526 Shi, Q., Bourassa, M. A., (2019), Coupling Ocean Currents and Waves with Wind Stress  
527 over the Gulf Stream, *Remote Sensing*, 11, 1476, doi:10.3390/rs11121476

528 Simmen, J. A., Saffman, P. G., (1985), Steady deep-water waves on a linear shear current,  
529 *Studies in Applied Mathematics*, 73, 35–57, doi: 10.1002/sapm198573135

530 Takagaki, N., Komori, S., Suzuki, N., Iwano, K., Kuramoto, T., Shimada, S., Kurose, R.,  
531 Takahashi, K., (2012), Strong correlation between the drag coefficient and the  
532 shape of the wind sea spectrum over a broad range of wind speeds, *Geophysical*  
533 *Research Letters*, 39, doi:10.1029/2012GL053988. L23604

534 Takagaki, N., Komori, S., Suzuki, N., Iwano, K., Kurose, R., (2016), Mechanism of drag  
535 coefficient saturation at strong wind speeds, *Geophysical Research Letters*, 43,  
536 doi:10.1002/2016GL070666

537 Takagaki, N., Komori, S., Ishida, M., Iwano, K., Kurose, R., Suzuki, N., (2017),  
538 Loop-type wave-generation method for generating wind waves under long-fetch  
539 conditions, *Journal of Atmospheric Oceanic Technology*, 34(10), 2129–2139,  
540 doi:10.1175/JTECH-D-17-0043.1

541 Takagaki, N., Suzuki, N., Takahata, S., Kumamaru, H., (2020), Effects of air-side  
542 freestream turbulence on development of wind waves, *Experiments in Fluids*, 61,  
543 136, doi:10.1007/s00348-020-02977-9

544 Troitskaya, Y. I., Sergeev, D. A., Kandaurov, A. A., Baidakov, G. A., Vdovin, M. A.,  
545 Kazakov, V. I., (2012), Laboratory and theoretical modeling of air-sea momentum  
546 transfer under severe wind conditions, *Journal of Geophysical Research*, 117,  
547 C00J21, doi:10.1029/2011JC007778

548 Troitskaya, Y., Sergeev, D., Vdovin, M., Kandaurov, A., Ermakova, O., Takagaki, N.,  
549 (2020), Laboratory study of the effect of surface waves on heat and momentum  
550 transfer at strong winds, *Journal of Geophysical Research Oceans*, doi:  
551 10.1029/2020JC016276

552

553